

1 Thallium isotopes reveal protracted anoxia associated with
2 volcanism, carbon burial, and mass extinction during the
3 Toarcian (Early Jurassic)

4 **Theodore R. Them II^{a1}, Benjamin C. Gill^b, Andrew H. Caruthers^c, Angela M. Gerhardt^{b,d},**
5 **Darren R. Gröcke^e, Timothy W. Lyons^f, Selva M. Marroquín^b, Sune G. Nielsen^g, João P.**
6 **Trabucho Alexandre, and Jeremy D. Owens^a**

7 ^a*Department of Earth, Ocean and Atmospheric Science & National High Magnetic Field*
8 *Laboratory, Florida State University, Tallahassee, Florida 32306, USA*

9 ^b*Department of Geosciences, Virginia Polytechnic Institute and State University, Blacksburg,*
10 *Virginia 24061, USA*

11 ^c*Department of Geosciences, Western Michigan University, Kalamazoo, Michigan 49006, USA*

12 ^d*Enervest, Ltd, Houston, Texas 77002, USA*

13 ^e*Department of Earth Sciences, Durham University, Durham, DH1 3LE, UK*

14 ^f*Department of Earth Sciences, University of California, Riverside, California 92521 USA*

15 ^g*Department of Geology and Geophysics, Woods Hole Oceanographic Institution, Woods Hole,*
16 *Massachusetts 02543, USA*

17 ^h*Department of Earth Sciences, Universiteit Utrecht, P. O. Box 80115 3508 TC Utrecht, The*
18 *Netherlands*

19 ¹Corresponding author: tthem@fsu.edu

23 PHYSICAL SCIENCES: Earth, Atmospheric, and Planetary Sciences

24

25

26

27

28

29

30

31

32

33

34

35

36

37

38

39

40

41

42

43

44

45

46 For this study, we generated thallium (Tl) isotope records from two anoxic basins to track
47 the earliest changes in global bottom water oxygen contents over the Toarcian Oceanic
48 Anoxic Event (T-OAE) of the Early Jurassic (~183 Ma). The T-OAE, like other Mesozoic
49 OAEs, has been interpreted as an expansion of marine oxygen depletion based on indirect
50 methods such as organic-rich facies, carbon isotope excursions, and biological turnover. Our
51 Tl isotope data, however, reveal explicit evidence for earlier global marine deoxygenation of
52 ocean water, some 600 ka before the classically defined T-OAE. This antecedent
53 deoxygenation occurs at the Pliensbachian/Toarcian boundary and is coeval with the onset
54 of initial large igneous province (LIP) volcanism and the initiation of a marine mass
55 extinction. Thallium isotopes are also perturbed during the T-OAE interval, as defined by
56 carbon isotopes, reflecting a second deoxygenation event that coincides with the acme of
57 elevated marine mass extinctions and the main phase of LIP volcanism. This suggests that
58 the duration of widespread anoxic bottom waters was at least one million years in duration
59 and spanned early to middle Toarcian time. Thus, the Tl data reveal a more nuanced record
60 of marine oxygen depletion and its links to biological change during a period of climatic
61 warming in Earth's past and highlights the role of oxygen depletion on past biological
62 evolution.

63

64 **Keywords:** Toarcian Oceanic Anoxic Event; Early Jurassic; Thallium isotopes; carbon isotope
65 excursion; large igneous province; mass extinction

66

67

68

69 **Significance Statement**

70 Declining oxygen contents in today's oceans highlight the need to better understand
71 ancient, natural marine deoxygenation and associated extinctions. In the Early Jurassic, the
72 Toarcian Oceanic Anoxic Event (T-OAE; ~183 Ma) is associated with significant perturbations to
73 the Earth system, historically defined by carbon isotopes. We reconstructed global oceanic
74 (de)oxygenation using thallium isotopes from two ocean basins that suggest a stepwise decline of
75 oxygen that initiated before and extended well after the classically defined T-OAE interval. This
76 initial deoxygenation occurs with the start of massive volcanism and marine extinctions while a
77 later shift corresponds to the traditional T-OAE. This emphasizes the need for more nuanced
78 records of ancient environmental and biogeochemical feedbacks that lead to and maintain
79 widespread marine anoxia.

80

81

82 **Introduction**

83 The amount of oxygen dissolved in the modern ocean is decreasing (1, 2), due in part to
84 the increasing concentration of greenhouse gases in the atmosphere. Similar scenarios have likely
85 occurred throughout geologic history. For example, during transient intervals in the Mesozoic—
86 known as oceanic anoxic events (or OAEs)—substantial increases in atmospheric greenhouse
87 gases are linked to the volcanic emissions of large igneous provinces (LIPs); these changes are
88 hypothesized as the primary driver of OAEs (3–5). Understanding the mechanisms underlying
89 intervals of marine deoxygenation in Earth history, such as OAEs, is essential because they are
90 intimately linked with ecological shifts and specifically marine mass extinctions (6). Additionally,
91 they provide us with an analog for possible future changes in the long-term oxygen inventory of

92 the ocean of our planet (7, 8).

93 The concept of an OAE was proposed by ref. 9 to explain the multiple ocean basin
94 occurrences of coeval organic-matter-rich sediments, or black shales, deposited at a wide range of
95 water depths on the middle Cretaceous ocean floor. OAEs were defined as brief (<1 Ma) episodes
96 of expansion and intensification of the oxygen minimum layer in the ocean. This expanding layer
97 encroached on the seafloor of seamounts, submarine plateaus, and continental margins and resulted
98 in enhanced burial of organic matter in widespread black shales. The broad temporal association
99 of these black shales with positive excursions in the marine carbon isotope record was
100 subsequently documented (10). These excursions have been interpreted to reflect the elevated
101 burial of ¹³C-depleted organic carbon during the OAE (e.g., 4, 5, 10–16). The concept of an OAE
102 was later applied to a positive excursion in the carbon isotope record of Tethyan Lower Jurassic
103 limestones during what is now known as the Toarcian OAE (15).

104 Subsequent studies of the Toarcian OAE identified an abrupt, large magnitude, negative
105 carbon isotope excursion (CIE) at ca. 183.1 Ma that interrupts a broader positive CIE noted by ref.
106 15. Generally, this negative CIE appears to define the onset of major environmental disruption,
107 the onset of organic-rich deposition, and the main pulse of mass extinction (5, 17–19) (Fig. 1). A
108 carbon isotope compilation of published work has also shown that the broader early Toarcian
109 positive CIE actually begins at the Pliensbachian/Toarcian boundary (Fig. 1, SI Fig. 3) (5, 20, 21).
110 However, this broader positive CIE precedes the onset of organic-rich deposition that defines the
111 start of the T-OAE at many locations (5, 16, and many others) (Fig. 1, SI Fig. 3, SI Text) (Fig. 1),
112 thus it has not been generally considered part of the T-OAE. This interval is also intriguing because
113 it corresponds to the beginning of a mass extinction that later reaches its climax during the T-OAE
114 (19).

115 Although positive CIEs could represent the effects of large-scale oxygen depletion in
116 seawater, other environmental variables can contribute to the carbon isotope record (22, 23), and
117 there is no simple relationship between redox conditions and organic matter preservation (24, as
118 reviewed by ref. 25). Thus, the culmination of a positive CIE does not require global ocean
119 deoxygenation or even increased organic carbon burial (22, 24–27), as carbon isotopes ultimately
120 track the balance of all the input and output fluxes and associated isotope fractionations (22). For
121 this reason, carbon isotope data cannot be used alone as a proxy for the expansion of oceanic
122 anoxia. Additionally, evidence for decreasing marine oxygen inventories leading to OAEs is
123 hampered since redox proxies typically constrain the most extreme euxinic (oxygen-free, sulfide-
124 containing waters) end member (28–31). As such, uniquely constraining the global extent of non-
125 sulfidic, anoxic waters has not been possible. This bias highlights the need for a more sensitive
126 proxy that constrains more subtle changes in oceanic oxygen levels during OAEs and other
127 oceanographic events in Earth history.

128

129 **Using thallium isotopes to track global marine oxygen contents**

130 Thallium isotopes in organic-matter-rich mudstones provide a novel window to secular
131 variations in the oceanic oxygen inventory over the expanded T-OAE interval from the latest
132 Pliensbachian to middle Toarcian (see Supplemental Information for Tl isotope nomenclature).
133 The modern open ocean seawater Tl isotope composition (with a residence time of ca. 20 ka) is
134 homogenous to within $< 0.5 \epsilon$ -units (32–34), and this seawater value is captured in the sediments
135 deposited in euxinic settings (34). Thallium is introduced to the ocean by rivers, high-temperature
136 hydrothermal fluids, volcanic emissions, mineral aerosols, and pore-water fluxes from continental-
137 margin sediments. These sources have essentially identical Tl isotopic compositions of $\epsilon^{205}\text{Tl} \sim -2$

138 (as reviewed in ref. 35), which reflects minimal isotope fractionation during continental
139 weathering and high-temperature mobilization of Tl. The major outputs of Tl from the marine
140 system include adsorption onto manganese (Mn)-oxides and, low-temperature (<100°C) alteration
141 of oceanic crust (AOC). Sedimentation of organic matter and sulfide minerals in low oxygen
142 settings also removes Tl from seawater, but the global flux is relatively minor in the modern ocean
143 (34, 36). Adsorption onto Mn-oxides and AOC are the only known processes that fractionate Tl.

144 Specifically, Mn oxides are heavier than seawater by $\sim+13-19$ ϵ -units, which is likely due
145 to equilibrium isotope fractionation during oxidation of univalent aqueous Tl to trivalent Tl when
146 permanently sorbed to Mn oxides (35, 37, 38). The uncertainty associated with the Tl isotope
147 fractionation factor during sorption to Mn oxides relates to Tl isotope variations found in some
148 pelagic clays with somewhat less positive compositions (39). However, pure Mn oxides as found
149 in Fe-Mn crusts display relatively constant offsets from seawater of $\sim+19\pm 2$ ϵ -units (32, 35), which
150 is the preferred value for Tl isotope fractionation during sorption to Mn oxides.

151 The mechanism of Tl isotope fractionation during incorporation into AOC is less well
152 understood but is likely a kinetic process whereby the light isotope is preferentially incorporated
153 into AOC (35). Although individual samples of AOC can exhibit $\epsilon^{205}\text{Tl} \sim -15$ (40) the average is
154 more likely closer to $\epsilon^{205}\text{Tl} \sim -7$ because uptake is close to quantitative from the circulating
155 hydrothermal fluids (35), thus the fractionation from seawater is minimal.

156 Although the marine Tl residence time is long enough to produce a globally homogenous
157 Tl isotope composition of the ocean it is still short enough that seawater $\epsilon^{205}\text{Tl}$ can respond to rapid
158 global changes in Mn-oxide burial on glacial-interglacial timescales (35; 41). In contrast, AOC
159 deposition rates vary on extremely long timescales ($>10^7$ years) as it responds primarily to global
160 average ocean crust production rates (42) and, hence, $\epsilon^{205}\text{Tl}_{\text{seawater}}$ variations on timescales shorter

161 than ~1 million years are most likely driven by changes in Mn-oxide preservation and burial.
162 Crucially, Mn-oxides are only buried in sediments with O₂ present at or near the sediment/water
163 interface because they are rapidly dissolved under anoxic conditions (43). In turn, global Mn-oxide
164 burial fluxes are related to the global extent of bottom water anoxia (34). As such, $\epsilon^{205}\text{Tl}_{\text{seawater}}$ can
165 be related to relative changes in oceanic oxygenation. Thallium isotopes have been applied to only
166 one ancient climate perturbation that documents the global relationship between oceanic
167 oxygenation leading up to the Cenomanian-Turonian event of OAE 2 (41), and it was shown that
168 changes in carbon isotopes lagged the onset of marine deoxygenation, which underlines the
169 potential for Tl isotopes to provide unique information about ancient oceanic oxygenation. During
170 intervals of increased bottom water oxygen extent, $\epsilon^{205}\text{Tl}_{\text{seawater}}$ values will be more negative,
171 whereas during intervals of decreased bottom water oxygen extent (increase of bottom water
172 anoxia), $\epsilon^{205}\text{Tl}_{\text{seawater}}$ values will be more positive and approach their source value ($\epsilon^{205}\text{Tl} = \sim -2$).

173

174 **Study site selection**

175 To reconstruct global ocean oxygen contents (or redox changes) using the Tl isotope
176 system, it is necessary to constrain local water column redox conditions to be sure to capture the
177 seawater value, thus avoiding any local Mn-oxide signatures. This is because variations in local
178 sedimentary redox conditions and basinal restriction can influence the isotopic signals captured in
179 the sedimentary record and can hamper the use of these records to reconstruct changes in global
180 marine redox conditions (31, 36, 45, 46). Therefore, it is important to investigate multiple localities
181 that were well-connected to the open ocean and have independent constraints on local redox
182 conditions (e.g., 41, 47). Here, we analyzed samples from two Lower Jurassic successions that
183 contain intervals that were deposited under euxinic conditions—as identified by established,

184 independent proxies for local redox, including Fe speciation—before, during, and after the T-OAE
185 (Fig. 2 and SI Figs. 1, 2). We first investigated three Pliensbachian and Toarcian sections of the
186 Fernie Formation from the Western Canada Sedimentary Basin, which represent deposition on an
187 open-ocean margin of northeastern Panthalassa (Fig. 2). These samples were taken from outcrop
188 (East Tributary) and two cores (1-35-62-20W5, 6-32-75-5W6). The other studied Toarcian
189 succession, Dotternhausen Quarry, Germany, represents deposition in a semi-restricted structural
190 basin in the European epeiric sea, which was connected to the Tethys Ocean (48) (Fig. 2).

191

192 **Results**

193 Data from the base of the East Tributary section, within the Pliensbachian portion of the
194 section (*Amaltheus margaritatus* ammonite Zone in Northwest Europe and *Fanninoceras kunea*
195 ammonite Zone in North America) start with a $\epsilon^{205}\text{Tl}$ of ~ -6 (Fig. 3). These values are similar to
196 the $\epsilon^{205}\text{Tl}$ of modern seawater (34) and suggest a similar global Tl isotopic mass balance tied to
197 Mn-oxide burial and similar extents of oxygenated bottom waters. At the Pliensbachian/Toarcian
198 boundary, $\epsilon^{205}\text{Tl}$ gradually shifts to less negative values and remains steady until the onset of the
199 negative Toarcian CIE. We interpret this initial rise in $\epsilon^{205}\text{Tl}$ as the beginning of the expansion of
200 oceanic anoxia before the classically defined T-OAE (see Fig. 1) with a date of ~ 183.65 Ma (\pm
201 ~ 0.150 Ma) (49)—approximately 500–600 kyr before the onset of the negative CIE (50, 51) that
202 traditionally defines the base of the T-OAE. Furthermore, our $\delta^{13}\text{C}$ and $\epsilon^{205}\text{Tl}$ data from two drill
203 cores from elsewhere in the Western Canada Sedimentary Basin show similar values and trends
204 (see SI Figs 1 and 2), suggesting that they capture global signals and that Early Jurassic seawater
205 $\epsilon^{205}\text{Tl}$ values are also homogenous.

206 The German Dotternhausen Quarry section (31, 48), where the Pliensbachian/Toarcian

207 boundary is not present, shows time-equivalent $\epsilon^{205}\text{Tl}$ values (~ -4) that are nearly identical, within
208 analytical error, to results from Canada (~ -3.5) for the lower Toarcian *Dactyloceras tenuicostatum*
209 (equivalent) ammonite Zone (Fig. 3). The $\epsilon^{205}\text{Tl}$ values increase at the onset of the negative CIE,
210 gradually decrease during the minimum of the CIE, and increase during the rising limb of the
211 carbon isotope data (Fig. 3). A longer-term decrease of Tl isotopes occurs after the end of the
212 negative CIE to the top of the section (Fig. 3). The similarities among all the study sites support
213 the interpretation that these Tl isotope records represent primary global ocean signals, even in the
214 more restricted setting of the German section.

215

216 **Discussion**

217 The shift in Tl isotopes from -6 to -4, as observed at the Pliensbachian/Toarcian boundary
218 (Fig. 3), based on isotope mass balance calculations, requires a $\sim 50\%$ decrease in the global burial
219 of Mn-oxides (34). In all likelihood, the decline in marine Mn-oxide burial was linked to an
220 expansion of bottom water anoxia, which restricted the area of oxic sediment deposition. This
221 initial deoxygenation is notable because it generally coincides with 1) the interpreted onset of
222 Karoo-Ferrar LIP activity (52, 53) at the start of the longer-term positive CIE, 3) initiation of a
223 radiogenic osmium isotope excursion (49, 54), and 4) the beginning of a major marine extinction
224 event (beginning of Phase 3 of ref. 19) (Fig. 4). These observations are consistent with marine
225 deoxygenation caused by an increase in organic carbon export linked to enhanced chemical
226 weathering and nutrient input to the oceans. This sequence led to increased oxygen consumption
227 in the aphotic zone—driving the expansion of oxygen minima in the ocean that is recorded by Tl
228 isotopes. The $^{187}\text{Os}/^{188}\text{Os}_i$ values decline soon after the Pliensbachian/Toarcian boundary (49, 54),
229 suggesting that the rate of continental weathering declined. Thus, the sustained deoxygenation and

230 elevated organic carbon burial (Figs. 3 and 4), evidenced by the thallium and carbon isotope
231 records, respectively, were mediated by processes internal to the oceans rather than the continued,
232 elevated supply of nutrients from rivers. Such internal processes could be lower oxygen solubility,
233 changes in ocean circulation under a warming climate, and/or the enhanced recycling of bio-
234 essential nutrients, such as phosphorus, under more reducing conditions.

235 The Tl isotope trends during the negative CIE (i.e., the traditional T-OAE interval) also
236 suggest that global bottom water redox did not remain constant over the event. The shift from -3.5
237 to -2 and a return to -3.5, observed both in Canada and Germany, indicate another deoxygenation
238 event and decrease in the global burial of Mn-oxides (Fig. 3). This perturbation likely occurred
239 over approximately 30 to 50 kyr assuming the timescale of refs. 50 and 55 (the T-OAE negative
240 CIE has been assigned a duration of ~300 to 500 kyr, which locally is represented in ~4.5m in
241 Alberta) and linear sedimentation rates in Canada (from 11.345 to 11.84 m in the section) (49).
242 The continued positive shift in the Tl isotope data during the recovery limb of the negative CIE of
243 the T-OAE would require further marine deoxygenation and an additional ~25% reduction in
244 global Mn-oxide burial (34). The dissolution of Mn-oxides could be driven by permanent anoxia
245 or more realistically, transient deoxygenation that includes seasonal, centennial, and/or longer
246 timescales depending on local hydrography, water chemistry, and sedimentation rates. Both the
247 Pliensbachian/Toarcian Boundary and the onset of the traditional T-OAE interval are associated
248 with increased Mn/Ca values (56, 57), which could be due to the increased dissolved Mn reservoir
249 associated with the dissolution of Mn-oxides and reduction of Mn-oxide precipitation.

250 The traditional T-OAE interval (i.e., as defined by the negative CIE) is associated with the
251 main phase of Karoo-Ferrar LIP magmatism (50, 52, 58). This magmatic pulse would have caused
252 global warming and enhanced continental weathering, as suggested by numerical modeling and

253 geochemical and sedimentological records (49, 54, 59, 60). The net result would have been marine
254 eutrophication and intensified and more widespread oxygen minima (e.g., 5, 49, 60). The second
255 $\epsilon^{205}\text{Tl}$ shift during the rising limb of the T-OAE CIE is roughly coincident with previously
256 interpreted maximum extents of water-column sulfidic anoxia (i.e., euxinia) during this event (31,
257 61). This second deoxygenation event corresponds to a further decline in marine diversity (end of
258 phase 3 in ref. 19)—that is, a continuation and ultimately the acme of the event that started at the
259 Pliensbachian/Toarcian boundary (17, 18, 62–64) (Fig. 4). Given that these major losses in marine
260 diversity occur coincidentally with changes observed in the Tl isotope record (Fig. 4), ocean
261 deoxygenation is implied as a significant or even the ultimate driver of extinction during this time.
262 This interpretation does not, however, preclude a role by other environmental changes that may
263 have occurred over this time in response to increasing $p\text{CO}_2$ (e.g., global warming and ocean
264 acidification).

265 Interestingly, the $\epsilon^{205}\text{Tl}$ data do not immediately return to pre-event values after the peak
266 of the positive CIE and remain high through the *Harpoceras falciferum* and lower *Hildoceras*
267 *bifrons* ammonite Zones as $\delta^{13}\text{C}$ declines (Fig. 3). A similar pattern has been observed in the Tl
268 isotope record of OAE-2 marked by values that remain high well after the end of the positive CIE
269 (38). The decoupling of the two isotope systems suggests that global Mn-oxide burial remained
270 low and bottom-water oxygen minima continued well after the termination of globally enhanced
271 organic carbon burial rates during both OAEs.

272 One interpretation for this observation could be that while overall organic carbon burial
273 declined, productivity was sufficiently high to maintain the consumption of deeper water oxygen
274 renewal (41). This scenario seems to be supported by the Os isotope record, which also remains
275 elevated above pre-event values over this same interval (49, 54) and indicates continued elevated

276 continental weathering rates. Thus, the continued enhanced delivery of nutrients from weathering
277 on the continents would have fueled elevated primary production that could have maintained the
278 widespread expanded marine anoxia. Alternatively, large amounts of near-surface organic matter
279 previously deposited during the event could have continued to drive bottom-water oxygen
280 consumption and Mn-oxide dissolution during a time when new organic matter burial waned. This
281 mechanism may also explain the elevated rates of pyrite burial inferred from the carbonate-
282 associated-sulfate sulfur isotope records that persist well after the CIE in both the T-OAE (61) and
283 OAE-2 (65). Consumption of organic matter in shallowly buried sediments might have fueled
284 marine anoxia and pyrite burial well after the CIEs, irrespective of the flux of newly exported
285 organic matter.

286

287 **Conclusions**

288 The Tl isotope data presented here reveal a more nuanced and explicit evidence for marine
289 deoxygenation in the interval that surrounds the T-OAE, which began at the
290 Pliensbachian/Toarcian boundary and expanded oxygen minima were sustained throughout the
291 early Toarcian and well after the traditionally defined T-OAE interval. Since the Tl isotope
292 excursion begins at the Pliensbachian/Toarcian boundary and generally corresponds with 1) the
293 initiation of massive volcanism, 2) a brief but significant increase in continental weathering, and
294 3) the start of the protracted early Toarcian mass extinction event (19). Thus, this evidence for
295 global marine deoxygenation provides a mechanism for the observed extinction record. Further,
296 the current definition of the beginning of T-OAE, based on the start of the negative CIE and/or
297 first occurrence of black shales in Europe, represents the nadir of the deterioration of
298 environmental conditions, but not the onset of global deoxygenation.

299 The concept of an OAE was proposed due to the realization that the preservation of organic
300 matter in marine sediments might not always be the product of local conditions. It followed that
301 carbon isotope excursions became the signature of enhanced burial of organic carbon on a global
302 scale. Our study highlights the need to revisit our definition of the temporal OAE and consider
303 whether for the record of oceanic anoxia might be better defined by other geochemical proxies that
304 reconstruct specific redox states of the global ocean. Perhaps more importantly, the
305 acknowledgment that global deoxygenation may expand beyond the traditionally defined OAEs
306 has important implications for our understanding of the environmental feedbacks that lead to and
307 maintain these events. Identifying such processes would be key to determining the consequences
308 and potential endpoints of the recent trend in deoxygenation in the oceans today.

309

310 **ACKNOWLEDGMENTS**

311 TRT would like to thank the FSU Arts and Sciences Postdoctoral Fellowship, GSA, AAPG,
312 SEPM, and Virginia Tech for funding. Grants to BCG (NSF EAR-1324752), JDO and SGN (NSF
313 OCE-1624895 and NASA NNX16AJ60G), and TWL (NSF EAR-0719911) also funded this work.
314 A portion of this work was performed at the National High Magnetic Field Laboratory, which is
315 supported by National Science Foundation Cooperative Agreement No. DMR-1157490 and the
316 State of Florida. We thank Hannah Grove, Brett Holdaway, and Ashley Prow for laboratory
317 assistance. Alberta outcrop collections were authorized by the following permits: Parks Canada,
318 Permit No: YHTR-2014-16156; RTMP, Permit No: 13-058, 14-009, 15-019. Finally, we would
319 like to thank two anonymous reviewers whose comments greatly improved the manuscript.

320

321 **Author Contributions**

322 TRT, BCG, and JDO designed the study. TRT, AHC, AMG, BCG, and SMM collected
323 samples. AHC identified the ammonites. TRT, BCG, SMM, and JDO conducted the geochemical
324 analyses. TRT wrote the paper with significant contributions from all the authors.

325

326

327 **References and Notes:**

328 1. Schmidtko S, Stramma L, Visbeck M (2017) Decline in global oceanic oxygen content during
329 the past five decades. *Nature* 542:335–339.

330 2. Breitburg D, et al. (2018) Declining oxygen in the global ocean and coastal waters. *Science*
331 359:eaam7240.

332 3. Pálffy J, Smith PL (2000) Synchrony between Early Jurassic extinction, oceanic anoxic event,
333 and the Karoo-Ferrar flood basalt volcanism. *Geol* 28:747–750.

334 4. Takashima R, Nishi H, Huber, BT, Leckie RM (2006) Greenhouse world and the Mesozoic
335 ocean. *Ocean* 19:64–74.

336 5. Jenkyns HC (2010) Geochemistry of oceanic anoxic events. *Geochem Geophys Geosys*
337 11:Q03004.

338 6. Rothman DH (2017) Thresholds of catastrophe in the Earth system. *Sci Adv* 3:e1700906.

339 7. Keeling RF, et al. (2010) Ocean deoxygenation in a warming world. *Ann Rev Mar Sci* 2:199–
340 229.

341 8. Long MC, et al. (2016) Finding forced trends in oceanic oxygen. *Glob Biogeochem Cyc*
342 30:381–397.

343 9. Schlanger SO, Jenkyns HC (1976) Cretaceous Oceanic Anoxic Events: Causes and
344 Consequences. *Geol Mijn* 55:179–184.

- 345 10. Scholle PA, Arthur MA (1980) Carbon Isotope Fluctuations in Cretaceous Pelagic
346 Limestones: Potential Stratigraphic and Petroleum Exploration Tool. *Am Assoc Petr Geol*
347 *Bull* 64:67–87.
- 348 11. Schlanger SO, Arthur MA, Jenkyns HC, Scholle PA (1987) The Cenomanian-Turonian
349 Oceanic Anoxic Event, I. Stratigraphy and distribution of organic carbon-rich beds and the
350 marine $\delta^{13}\text{C}$ excursion. *Mar Pet Sour Rocks*, eds Brooks J, Fleet AJ (Geological Society,
351 London) Special Publications, Vol 26, pp 371–399.
- 352 12. Arthur MA, Dean WE, Pratt LM (1988) Geochemical and climatic effects of increased
353 marine organic carbon burial at the Cenomanian/Turonian boundary. *Nature* 335:714–717.
- 354 15. Jenkyns HC (1988) The early Toarcian (Jurassic) Anoxic Event: Stratigraphic, sedimentary,
355 and geochemical evidence. *Am J Sci* 19:101–151.
- 356 16. Hesselbo SP, et al. (2000) Massive dissociation of gas hydrate during a Jurassic oceanic
357 anoxic event. *Nature* 406:392–395.
- 358 17. Harries PJ, Little CTS (1999) The early Toarcian (Early Jurassic) and the Cenomanian-
359 Turonian (Late Cretaceous) mass extinctions: similarities and contrasts. *Palaeogeo*
360 *Palaeoclim Palaeoecol* 154:39–66.
- 361 18. Dera G, et al. (2010) High-resolution dynamics of Early Jurassic marine extinctions: the case
362 of Pliensbachian-Toarcian ammonites (Cephalopoda). *J Geol Soc Lon* 167:21–33.
- 363 19. Caruthers AH, Smith PL, Gröcke DR (2013) The Pliensbachian-Toarcian (Early Jurassic)
364 extinction, a global multi-phased event. *Palaeogeo Palaeoclim Palaeoecol* 386:104–118.
- 365 20. Hermoso M, et al. (2009) Expression of the Early Toarcian negative carbon-isotope
366 excursion in separated microfactions (Jurassic, Paris Basin). *Earth Plan Sci Lett* 277:194–
367 203.

- 368 21. Them TR II, et al. (2017) High-resolution carbon isotope records of the Toarcian Oceanic
369 Anoxic Event (Early Jurassic) from North America and implications for the global drivers
370 of the Toarcian carbon cycle. *Earth Plan Sci Lett* 459:118–126.
- 371 22. Kump LR, Arthur MA (1999) Interpreting carbon-isotope excursions: carbonates and organic
372 matter. *Chem Geol* 161:181–198.
- 373 23. Tyson RV (2005) The “Productivity versus Preservation” controversy: Causes, flaws, and
374 resolution. *SEPM Spec Pub No 82. The Deposition of Organic-Carbon-Rich Sediments:
375 Models, Mechanisms, and Consequences.* pp 17–33.
- 376 24. Middelburg JJ, Vlug T, Jaco F, van der Nat, WA (1993) Organic matter mineralization in
377 marine sediments. *Glob Plan Ch* 1-2:47–58.
- 378 25. Burdige DJ (2007) Preservation of Organic Matter in Marine Sediments: Controls,
379 Mechanisms, and an Imbalance in Sediment Organic Carbon Budgets? *Chem Rev* 109:467–
380 485.
- 381 26. Canfield DE (1994) Factors influencing organic carbon preservation in marine sediments:
382 *Chem Geol* 114:315–329.
- 383 27. Hartnett HE, Keil RG, Hedges JI, Devol AH (1998) Influence of oxygen exposure time on
384 organic carbon preservation in continental margin sediments: *Nature* 391:572–574.
- 385 28. Schouten S, et al. (2000) Effects of an oceanic anoxic event on the stable carbon isotopic
386 composition of early Toarcian carbon. *Am J Sci* 300:1–22.
- 387 29. Pearce CR, Cohen AS, Coe AL, Burton, KW (2008) Molybdenum isotope evidence for
388 global ocean anoxia coupled with perturbations to the carbon cycle during the Early
389 Jurassic. *Geol* 36:231–234.

- 390 30. French KL, Sepúlveda J, Trabucho-Alexandre J, Gröcke DR, Summons RE (2014) Organic
391 geochemistry of the early Toarcian oceanic anoxic event in Hawsker Bottoms, Yorkshire,
392 England. *Earth Plan Sci Lett* 390:116–127.
- 393 31. Dickson AJ, et al. (2017) Molybdenum isotope chemostratigraphy and paleoceanography of
394 the Toarcian Oceanic Anoxic Event (Early Jurassic). *Paleocean* 32:813–829.
- 395 32. Rehkämper M, et al. (2002) Thallium isotope variations in seawater and hydrogenetic,
396 diagenetic, and hydrothermal ferromanganese deposits. *Earth Plan Sci Lett* 197:65–81.
- 397 33. Nielsen SG, Rehkämper M, Norman MD, Halliday AN, Harrison D (2006) Thallium isotopic
398 evidence for ferromanganese sediments in the mantle source of Hawaiian basalts. *Nature*
399 439:314–317.
- 400 34. Owens JD, Nielsen SG, Horner TJ, Ostrander CM, Peterson LC (2017) Thallium-isotopic
401 compositions of euxinic sediments as a proxy for global manganese-oxide burial. *Geochim*
402 *Cosmochim Acta* 213:291–307.
- 403 35. Nielsen SG, Rehkämper M, Prytulak J (2017) Investigation and application of thallium
404 isotope fractionation. *Rev Min Geochem* 82:759–798.
- 405 36. Nielsen SG, et al. (2011) Thallium isotopes in early diagenetic pyrite – A paleoredox proxy?
406 *Geochim Cosmochim Acta* 75:6690–6704.
- 407 37. Nielsen SG, et al. (2013) Towards an understanding of thallium isotope fractionation during
408 adsorption to manganese oxides. *Geochim Cosmochim Acta* 117:252–265.
- 409 38. Peacock CL, Moon EM (2012) Oxidative scavenging of thallium by birnessite: Explanation
410 for thallium enrichment and stable isotope fractionation in marine ferromanganese
411 precipitates. *Geochim Cosmochim Acta* 84:297–313.
- 412 39. Rehkämper M, Frank M, Halliday A. (2004) Cenozoic marine geochemistry of thallium

- 413 deduced from isotopic studies of ferromanganese crusts and pelagic sediments. *Earth Plan*
414 *Sci Lett* 219:77–91.
- 415 40. Nielsen, SG et al. (2006) Hydrothermal fluid fluxes calculated from the isotopic mass
416 balance of thallium in the ocean crust. *Earth Plan Sci Lett* 1-2:120–133.
- 417 41. Ostrander CM, Owens JD, Nielsen SG (2017) Constraining the rate of oceanic
418 deoxygenation leading up to a Cretaceous Oceanic Anoxic Event (OAE-2: ~94Ma). *Sci Adv*
419 3:e1701020.
- 420 42. Nielsen SG, et al. (2009) Thallium isotope evidence for a permanent increase in marine
421 organic carbon export in the early Eocene. *Earth Plan Sci Lett* 278:297–307.
- 422 43. Rue EL, Smith GJ, Cutter GA, Bruland KW (1997) The response of trace element redox
423 couples to suboxic conditions in the water column. *Deep Sea Res Part I: Ocean Res Pap*
424 44:113–134.
- 425 45. McArthur JM, Algeo TJ, vd Schootbrugge B, Li Q, Howarth RJ (2008) Basinal restriction,
426 black shales, Re-Os dating, and the Early Toarcian (Jurassic) oceanic anoxic event.
427 *Paleocean* 23:PA4217.
- 428 46. Bura-Nakić E, et al. (2018) Coupled U-Mo abundances and isotopes in a small marine
429 euxinic basin: Constraints on processes in euxinic basins. *Geochim Cosmochim Acta*
430 222:212–229.
- 431 47. Owens JD, Reinhard CT, Rohrssen M, Love GD, Lyons, TW (2016) Empirical links between
432 trace metal cycling and marine microbial ecology during a large perturbation to Earth's
433 carbon cycle. *Earth Plan Sci Lett* 449:407–417.
- 434 48. Röhl H-J, Schmid-Röhl A, Oschmann W, Frimmel A, Schwark L (2001) The Posidonia
435 Shale (Lower Toarcian) of SW-Germany: an oxygen-depleted ecosystem controlled by sea

- 436 level and palaeoclimate. *Palaeogeog Palaeoclim Palaeoecol* 169:273–299.
- 437 49. Them TR, et al. (2017) Evidence for rapid weathering response to climatic warming during
438 the Toarcian Oceanic Anoxic Event. *Sci Rep* 7:5003.
- 439 50. Sell B, et al. (2014) Evaluating the temporal link between Karoo LIP and climatic-biologic
440 events of the Toarcian Stage with high-precision U-Pb geochronology. *Earth Plan Sci Lett*
441 408:48–56.
- 442 51. Ruhl M, et al. (2016) Astronomical constraints on the duration of the Early Jurassic
443 Pliensbachian Stage and global climatic fluctuations. *Earth Plan Sci Lett* 455:149–165.
- 444 52. Moulin M, et al. (2017) Eruptive history of the Karoo lava flows and their impact on early
445 Jurassic environmental change. *J Geophys Res Sol Earth* 2011JB008210.
- 446 53. Xu W, et al. (2018) Magnetostratigraphy of the Toarcian Stage (Lower Jurassic) or the
447 Llandbedr (Mochras Farm) Borehole, Wales: basis for a global standard and implications
448 for volcanic forcing of palaeoenvironmental change. *J Geol Soc* jgs:2017-120.
- 449 54. Percival LME, et al. (2016) Osmium isotope evidence for two pulses of increased continental
450 weathering linked to Early Jurassic volcanism and climate change. *Geol* 44:759–762.
- 451 55. Boulila S, et al. (2014) Astronomical calibration of the Toarcian Stage: Implications for
452 sequence stratigraphy and duration of the early Toarcian OAE. *Earth Plan Sci Lett* 386:98–
453 111.
- 454 56. Hermoso M. et al. (2009) Global and local forcing of Early Toarcian seawater chemistry: A
455 comparative study of different paleoceanographic settings (Paris and Lusitanian basins).
456 *Paleocean* 24:PA4208.
- 457 57. Lu, Z, Jenkyns HC, Rickaby REM (2010) Iodine to calcium ratios in marine carbonate as a
458 paleo-redox proxy during oceanic anoxic events. *Geol* 38:1107–1110.

- 459 58. Burgess SD, Bowring SA, Fleming TH, Elliot DH (2015) High-precision geochronology
460 links the Ferrar large igneous province with early-Jurassic ocean anoxia and biotic crisis.
461 *Earth Plan Sci Lett* 415:90–99.
- 462 59. Dera G, Donnadieu Y (2012) Modeling evidence for global warming, Arctic seawater
463 freshening, and sluggish oceanic circulation during the Early Toarcian anoxic event.
464 *Paleocean* 27:PA2211.
- 465 60. Izumi K, Kemp DB, Itamiya S, Inui M (2018) Sedimentary evidence for enhanced
466 hydrological cycling in response to rapid carbon release during the early Toarcian oceanic
467 anoxic event. *Earth Plan Sci Lett* 481:162–170.
- 468 61. Gill BC, Lyons TW, Jenkyns HC (2011) A global perturbation to the sulfur cycle during the
469 Toarcian Oceanic Anoxic Event. *Earth Plan Sci Lett* 312:484–496.
- 470 62. Little CTS, Benton MJ (1995) Early Jurassic mass extinction: A global long-term event.
471 *Geol.* 23:495–498.
- 472 63. Aberhan M, Baumiller TK (2003) Selective extinction among Early Jurassic bivalves: A
473 consequence of anoxia. *Geol* 31:1077–1080.
- 474 64. Caswell BA, Coe AL, Cohen AS (2009) New range data for marine invertebrate species
475 across the early Toarcian (Early Jurassic) mass extinction. *J. Geol. Soc.* 166:859–872.
- 476 65. Owens JD, et al. (2013) Sulfur isotopes track the global extent and dynamics of euxinia
477 during Cretaceous Oceanic Anoxic Event 2. *Proc Nat Acad Sci* 110:18407–18412.
- 478 66. Scotese CR (2001) Atlas of Earth History PALEOMAP Project, Arlington, TX.
- 479 67. Dera G, et al. (2009) Water mass exchange and variations in seawater temperature in the NW
480 Tethys during the Early Jurassic: Evidence from neodymium and oxygen isotopes of fish
481 teeth and belemnites. *Earth Plan Sci Lett* 286:198–207.

482

483

484 **Fig. 1: A)** Idealized Pliensbachian and Toarcian carbon isotope stratigraphy (derived from multiple
485 $\delta^{13}\text{C}$ records from Europe and North America shown in SI Fig. 3). Note the long-term positive
486 CIE predating the negative CIE associated with the classic T-OAE interval.

487

488 **Fig. 2:** Global paleogeography of early Toarcian (modified from refs. 21, 49, 66). Black circles
489 represent the study areas. Dashed extent of the Karoo-Ferrar LIP shown in southern Pangaea. Dark
490 grey represents landmasses, light blue: shallow seas, and dark blue: open oceans. CPM = Central
491 Pangaeian Mountains.

492

493 **Fig. 3:** Chemostratigraphy of the Lower Jurassic Fernie Formation from East Tributary of Bighorn
494 Creek Alberta and of the Lower Jurassic Posidonia Shale from the Dotternhausen Quarry in
495 Germany. $\delta^{13}\text{C}_{\text{org}}$ = organic carbon isotopic compositions from refs. 21 and 31. $\text{Fe}_{\text{HR}}/\text{Fe}_{\text{T}}$ = amount
496 of highly reactive iron relative to total iron, and $\text{Fe}_{\text{Py}}/\text{Fe}_{\text{HR}}$ = amount of pyrite iron relative to highly
497 reactive iron (see SI Materials and Methods for discussion of this redox proxy). $\epsilon^{205}\text{Tl}$ = thallium
498 isotopic composition of seawater during deposition. Lithostratigraphic members of the Fernie
499 Formation, Stages of the Jurassic, and ammonite zonations for both northwestern Europe and
500 western North American shown to the left of the stratigraphic column (refer to ref. Them17a and
501 SI Text for the details of their placements). Vertical gray line in ^{205}Tl records are the modern
502 $^{205}\text{Tl}_{\text{SW}}$ composition of ~ -6 (34). Light gray $\epsilon^{205}\text{Tl}$ values in the German section are from
503 lithologies that are not ideal for metal isotope studies (low TOC < 0.3%), and we therefore do not
504 interpret these as primary oceanographic signals (see SI Text). Gray boxes represent CIE intervals.

505

506 **Fig. 4:** Sequence of events culminating in the Early Jurassic T-OAE (as delineated by changes in
507 the precipitation of manganese oxyhydroxides at the sediment-water interface, documented by
508 shifts in the $\epsilon^{205}\text{Tl}$ composition of anoxic sediments) and carbon burial event (as delineated by
509 changes to the global carbon cycle, documented by changes in the $\delta^{13}\text{C}$ of organic and inorganic
510 carbon). As the Karoo-Ferrar LIP is emplaced (3, 52, 57), global ocean deoxygenation may occur
511 concurrently as sea surface temperatures rise (67). Massive injections of greenhouse gases and
512 cascading biogeochemical feedbacks cause the second decline in biodiversity associated with the
513 T-OAE negative CIE interval. The extent of anoxic marine bottom waters increases as
514 bioproductivity increases due to increased continental weathering and delivery of nutrients to the
515 oceans (49, 54), leading to the increased geographic extent of euxinia (31, 61), culminating in an
516 interval of maximum organic carbon burial, which causes the positive CIE. Increased oceanic
517 anoxia occurs concurrently with the onset of the main extinction event at the
518 Pliensbachian/Toarcian boundary (19, 63), and the greatest extent of anoxia and euxinia occurs
519 during the large, negative CIE interval (61, *this study*). White arrows represent “Phase 2” of the
520 Karoo-Ferrar eruptive scenario (52). Timescale is derived from ref. 51.

521

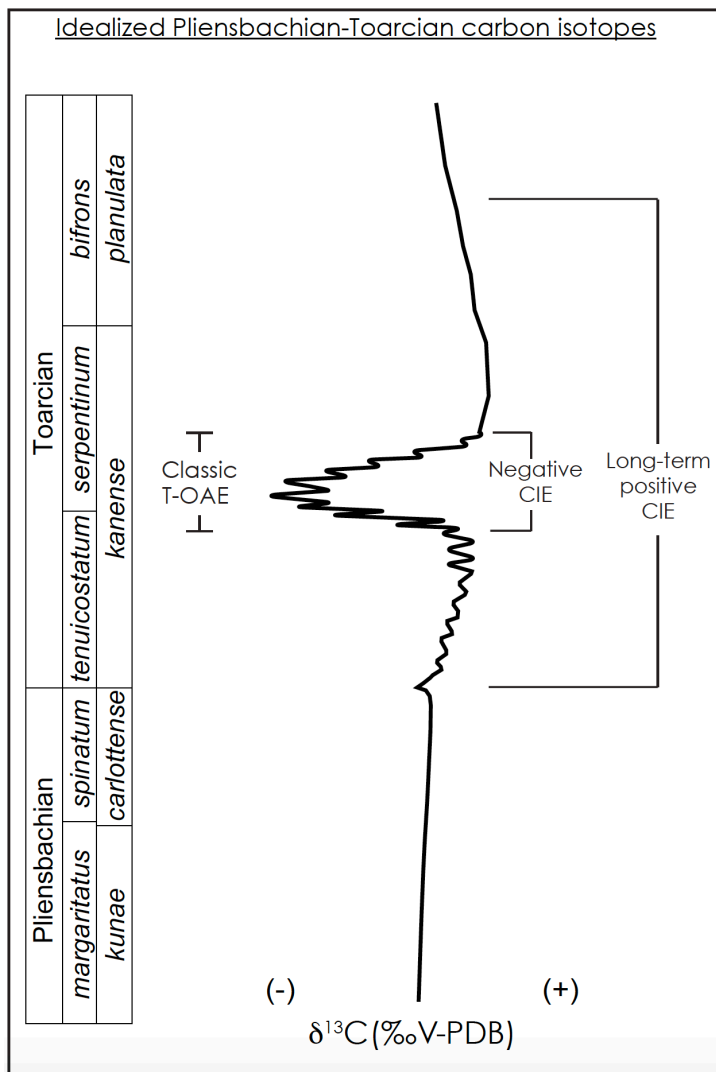
522

523 **Supplementary Materials:** Methods and Materials, Supplementary Text, Figures S1, S2, S3,
524 References, Databases S1 to S4.

525

526 **Additional Information**

527 **Competing financial interests:** The authors declare no competing financial interests



528

529 Fig. 1

530

531

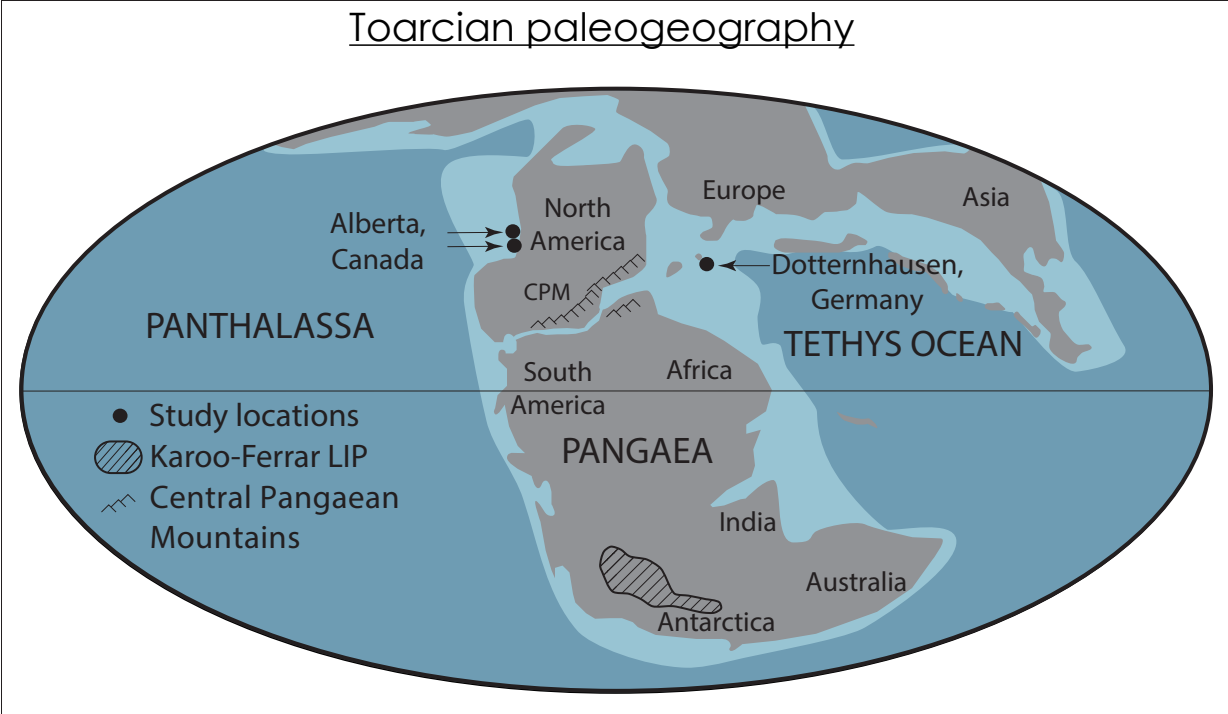
532

533

534

535

536



537

538 Fig. 2

539

540

541

542

543

544

545

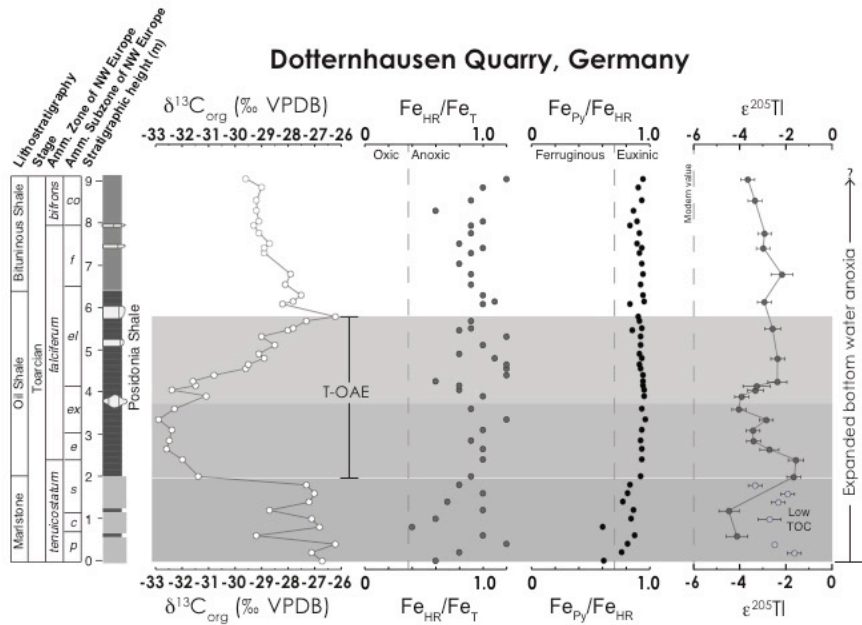
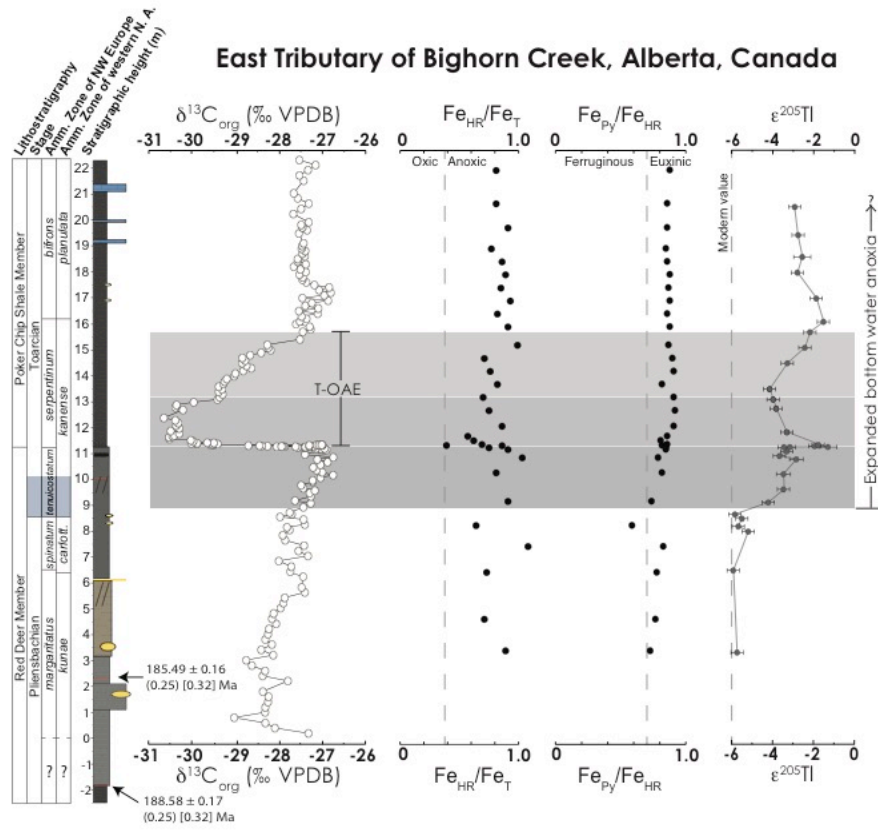
546

547

548

549

550

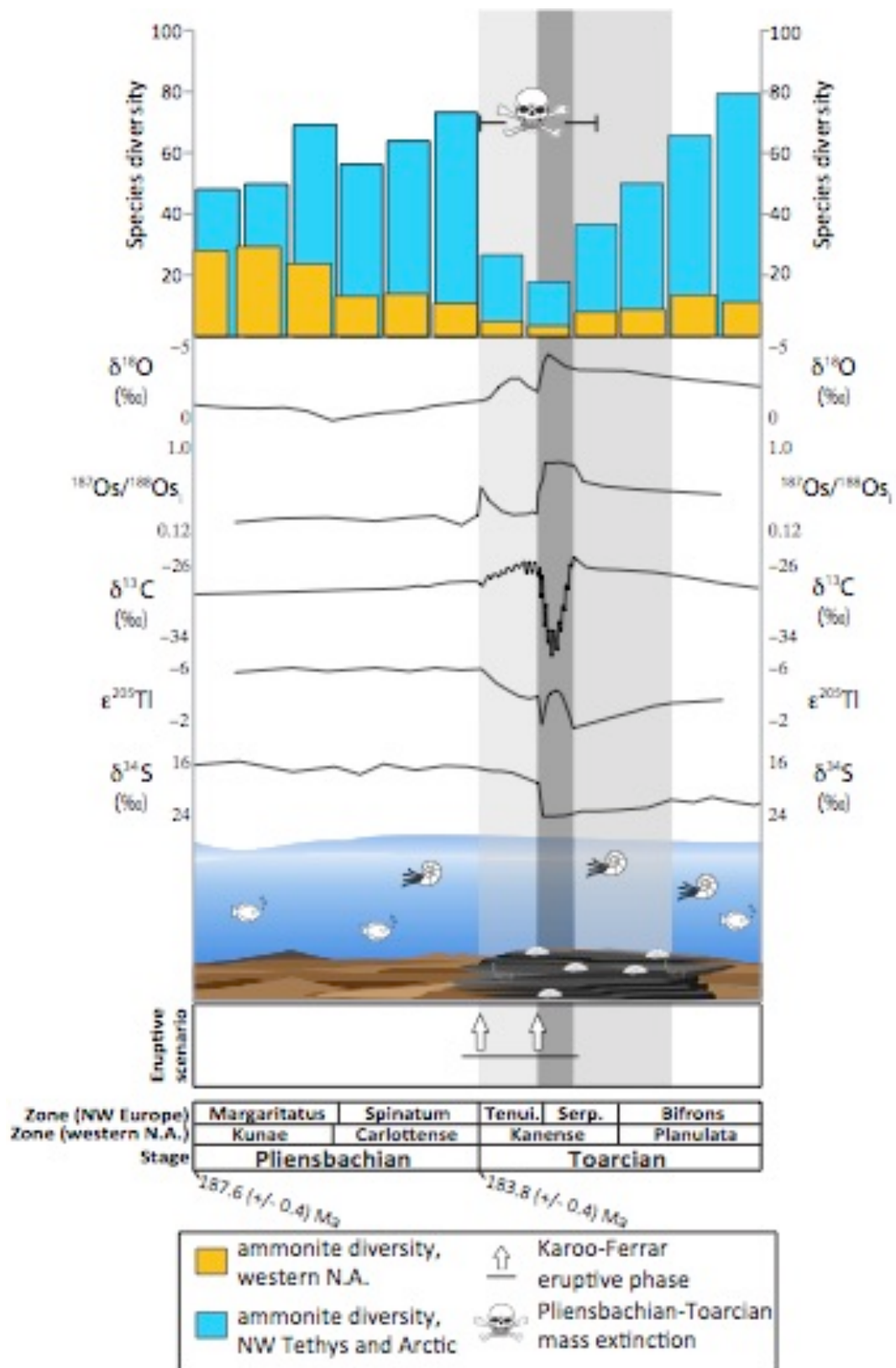


551

552 Fig. 3

553

554



555

556 Fig. 4

557
558
559 **Supplementary Materials for**
560 **Thallium isotopes reveal protracted anoxia associated with volcanism, carbon**
561 **burial and extinction during the Toarcian (Early Jurassic)**
562

563 Theodore R. Them II, Benjamin C. Gill, Andrew H. Caruthers, Angela M. Gerhardt, Darren R.
564 Gröcke, Timothy W. Lyons, Selva M. Marroquín, Sune G. Nielsen, João P. Trabucho Alexandre,
565 and Jeremy D. Owens
566

567 correspondence to: tthem@fsu.edu
568
569

570 **This PDF file includes:**
571

572 Materials and Methods
573 Supplementary Text
574 Figs. S1 to S3
575 References
576

577 **Other Supplementary Materials for this manuscript includes the following:**
578

579 Database S1: Geochemistry for East Tributary section.
580 Database S2: Geochemistry for drill core 1-35-62-20W5.
581 Database S3: Geochemistry for drill core 6-32-75-5W6.
582 Database S4: Geochemistry for Dotternhausen section.
583
584
585

586

587

588

589

590

591

592

593

594 **Materials and Methods**

595 Sampling Locations and Materials

596 Published accounts of the collective lithostratigraphy, ammonite biostratigraphy, U-Pb zircon age
597 dates, and high-resolution carbon isotope chemostratigraphy for the East Tributary and
598 Dotternhausen Quarry can be found in refs. 1, 2, 3, 4. Here, we discuss and summarize key aspects
599 of these analyses as they pertain to our study.

600 Drill cores 1-35-62-20W5 and 6-32-78-5W6 (SI Figs. 1, 2) of the Fernie Formation were
601 described and sampled for geochemical analyses at the Core Research Centre in Calgary, Alberta,
602 Canada. They contain the Pliensbachian to lower Toarcian Gordondale and Poker Chip Shale
603 (PCS) members, and have been correlated by geophysical gamma ray logs, ammonites, and carbon
604 isotopes to outcrops of Red Deer and PCS, including East Tributary (1, 5, 6). Each core contains
605 mixed organic-rich calcareous mudstones and siltstones in the Gordondale Member, which are
606 overlain by organic-rich calcareous mudstones of the PCS (5).

607 Core 1-35-62-20W5 contains alternating organic-rich calcareous siltstones and mudstones
608 (SI Fig. 1) of the Gordondale and PCS members. The Gordondale Member ranges from the base
609 of the core to 2029 m and contains several bivalve beds (5) and the Pliensbachian (Freboldi Zone)
610 ammonite *Dubariceras cf. silviesi* at 2033.3 m. The PCS Member comprises 2029 m to the top of
611 the core (5) and contains organic-rich calcareous mudstones, displacive and diagenetic carbonate
612 cements and fans, with abundant bivalves, the cephalopod *Atractites*, and the Toarcian ammonite
613 *Dactylioceras sp.* at 2027.1 m (5).

614 Core 6-32-78-5W6 contains alternating organic-rich calcareous siltstones and mudstones
615 (SI Fig. 2) of the Gordondale and PCS members. The Gordondale Member ranges from the base
616 of the core to ~1219 meters (5) and contains several bivalve beds⁵, the Pliensbachian ammonite
617 *Amaltheus sp.* at 1221.8 m, and Toarcian Kanense to Planulata Zone equivalent *Dactylioceras cf.*
618 *crossbeyi* and *Cleviceras exaratum* at 1217.9 and 1217.8 meters, respectively. From 1221 to 1219
619 m, the dominant lithology is an organic-rich mudstone, with a thin, organic-rich, silty mudstone
620 capped by a displacive carbonate fan around 1220.25 m. From 1219 to 1214.6 m, the dominant
621 lithology is an organic-rich, laminated, calcareous siltstone, with many bitumen-rich intervals. The
622 PCS Member comprises 1214.6 m to the top of the core (5) and contains organic-rich calcareous
623 mudstones, rare bivalves, and often contains intervals that are laminated.

624 These sections represent an excellent opportunity to use the Toarcian CIE as an intra-
625 basinal and a global chemostratigraphic marker (SI Fig. 3); since these cores represent time-
626 correlative, deeper-water facies to the East Tributary section (5), it is possible to reconstruct
627 paleoceanographic dynamics across the T-OAE. Specifically, if redox variations change with
628 paleo-water depth, and potentially temporally, then it should be possible to reconstruct the
629 temporal and spatial extent of oxygenation within the basin.

630

631 Total organic carbon contents (TOC) and isotope compositions ($\delta^{13}\text{C}_{\text{org}}$)

632 Carbon-isotope and total organic carbon content data of the East Tributary and
633 Dotternhausen sites were recently reported by refs. 1, 2 and ref. 4, respectively. The new data
634 presented here are from the 1-35-62-20W5 and 6-32-78-5W6 drill cores and follow the methods
635 in refs. 1, 2, 4.

636 Powders were obtained from the drill core and outcrops samples either using a handheld
637 Dremel tool with a diamond tip drill bit or a ball mill using a silica nitride ceramic vial set. To
638 remove the carbonate fraction, several milliliters of 2N HCl were added to ~0.1 g of powder and
639 allowed to react for ~24 hours. The solution was rinsed until a neutral pH was obtained, and then

640 the samples were dried in an oven.

641 $\delta^{13}\text{C}_{\text{org}}$ and total organic carbon (TOC) values of the carbonate-free sample residues were
642 conducted on an Isotope Cube elemental analyzer connected to an Isoprime 100 gas source isotope-
643 ratio mass spectrometer (IRMS) in the Sedimentary Geochemistry Isotope Laboratory in the
644 Department of Geosciences at Virginia Tech. The isotope compositions of the samples were
645 expressed in the standard delta (δ) notation as per mil deviations (‰) from Vienna Pee Dee
646 Belemnite (VPDB) and calculated such that:

$$647 \delta^{13}\text{C} = \left[\left(\frac{^{13}\text{C}/^{12}\text{C}}{\text{sample}} - \frac{^{13}\text{C}/^{12}\text{C}}{\text{standard}} \right) / \left(\frac{^{13}\text{C}/^{12}\text{C}}{\text{standard}} \right) \right] \times 1000 \quad \text{Eq. 1}$$

649 Samples were calibrated to the VPDB scale using international (IAEA-CH-6 and IAEA-
650 CH-7) and commercial standards (Elemental Microanalysis wheat flour, sorghum flour, low
651 organic soil, and urea). Long-term analytical precision for the $\delta^{13}\text{C}$ measurements is $<0.1\text{‰}$ based
652 on replicated analyses on isotope standards: this provided a linear range in $\delta^{13}\text{C}$ between -48.66‰
653 and -10.42‰ . Total organic carbon was obtained as part of the isotopic analysis using elemental
654 standards (i.e., Acetanilide, 71.09% C). Approximately 66% of total samples ($n = 86$) from core
655 6-32-78-5W6 were replicated at least once. Approximately 91% of total samples ($n = 78$) from
656 core 1-35-62-20W5 were replicated at least once. Average analytical uncertainty for replicated
657 analyses ($n = 128$) was 0.07‰ .

658

659 Iron speciation analysis

660 The amount of iron found in various mineral phases (iron speciation) of fine-grained
661 siliciclastic units can be used to identify local modern and ancient water column redox conditions
662 (7-10). Specifically, the amount highly reactive iron-bearing phases (Fe_{HR} ; see Equation 2) can be
663 quantified to determine local redox conditions during deposition (11). The Fe_{HR} pool represents
664 available iron that reacts with aqueous sulfide to form pyrite (12). The highly reactive iron pool
665 (e.g., 10) is defined as:

666

$$667 \text{Fe}_{\text{HR}} = \text{Fe}_{\text{py}} + \text{Fe}_{\text{carb}} + \text{Fe}_{\text{ox}} + \text{Fe}_{\text{mag}} \quad \text{Eq. 2}$$

668

669 where Fe_{py} represents iron bound as pyrite; Fe_{carb} represents iron hosted in carbonate phases
670 including calcite, siderite, and ankerite; Fe_{ox} represents iron hosted in the ferrihydrite,
671 lepidocrocite, goethite, and hematite fractions; and Fe_{mag} represents iron hosted in the magnetite
672 fraction.

673 Modern and ancient marine siliciclastic sediments deposited under an anoxic water column
674 have a $\text{Fe}_{\text{HR}}/\text{Fe}_{\text{T}}$ (Fe_{T} represents total iron in the sample) value of >0.38 , whereas sediments
675 deposited under an oxic water column are generally below 0.22 (7, 11, 13). Because the amount
676 of pyrite that can be deposited in anoxic environments during the microbial reduction of sulfate
677 (e.g., 12) can vary, the amount of Fe_{py} to Fe_{HR} in each sample can help discern whether the water
678 column was ferruginous (pyrite formation limited by available sulfides) or euxinic (pyrite
679 formation limited by available reactive iron). $\text{Fe}_{\text{py}}/\text{Fe}_{\text{HR}}$ values $> \sim 0.7-0.8$ are indicative of water
680 column euxinia, whereas $\text{Fe}_{\text{py}}/\text{Fe}_{\text{HR}}$ values $< \sim 0.7-0.8$ are indicative of ferruginous conditions (11,
681 14, 15).

682 To determine the relative amount of iron in each iron-bearing phase, the sequential
683 extraction method of ref. 8 was performed at the Department of Geosciences at Virginia Tech. For
684 this procedure, approximately 0.1 grams of powder was used. First, Fe_{carb} was liberated by the
685

686 addition of a 10mL solution of 1M sodium acetate and acetic acid, buffered to pH of 4. These
687 samples were placed on a shaking table for 48 hours at 50° C and then centrifuged. Next, Fe_{ox} was
688 liberated from the samples by the addition of a 10mL solution of sodium dithionite and sodium
689 citrate, buffered to pH of 4. These samples were placed on a shaking table for two hours, and then
690 centrifuged. Finally, Fe_{mag} was liberated by the addition of a 10mL solution of ammonium oxalate.
691 These samples were placed on a shaking table for six hours, and then centrifuged. After each
692 extraction, 100 µL of the supernatant was transferred to a new tube, followed by the addition of 4
693 mL of HEPES, ferrozine, and hydroxylamine HCl solution (e.g., 16) and allowed to react
694 overnight. All of the supernatant was removed in the original sample tubes before the next iron
695 extraction. Iron concentrations were measured in a spectrophotometer and calculated by a matrix-
696 matched standard curve (e.g., 17).

697 Fe_{py} values were determined by chromium reduction methods of ref. 18. For this procedure,
698 approximately 0.1 grams of powder was added to a three-neck flask for a distillation extraction.
699 Following the purging of headspace with nitrogen gas a solution of 40 mL of 1M chromous
700 chloride and 20 mL of 6N HCl was added to the flask, and then allowed to react for two hours
701 while heating under the nitrogen atmosphere. Any volatilized sulfide quantitatively reacted with a
702 zinc acetate solution to form zinc sulfide. Later, silver nitrate was added to this solution, which
703 converted the zinc sulfide to silver sulfide. The amount of sulfide in the sample was then
704 determined by gravimetry after filtration and drying of the silver sulfide. The amount of pyrite iron
705 hosted in the original sample was then stoichiometrically calculated from the amount of extracted
706 sulfide.

707 For the determination of Fe_T approximately 0.2 grams of powder was ashed at 900° C for
708 6-8 hours to remove any organic matter and other volatile phases. Approximately 0.1 grams of
709 powder was partially dissolved using 4 mL of 12M HCl, and then placed in a trace metal clean
710 Teflon Savillex digestion vessel on a hot plate and boiled for 36-48 hours (19). The sample and
711 solution were added to centrifuge tubes and centrifuged. After centrifugation, 100 µL of the
712 supernatant was transferred to a new tube and the same technique was used to measure iron
713 concentrations using a spectrophotometer as stated previously.

714 Iron concentrations were calculated by a matrix-matched standard curve. New standard
715 solutions were prepared for each analysis with iron standard concentrations at 0, 5, 10, 20, 30, 40
716 75, 150, and 300 ppm. The r² value of the standard curve was always above 0.999 and many
717 instances was 1. Multiple analyses of the same solution yielded no error via spectrophotometer
718 output, and no samples yielded higher iron concentrations than the standards. Sample
719 reproducibility using this method is often ± 7% when analyzing different aliquots of the same
720 extracted iron pool (e.g., 17).

721

722 Thallium isotope analysis

723 The precipitation of manganese oxides is directly controlled by available oxygen, and
724 therefore ceases in low oxygen environments. As manganese oxide precipitation decreases during
725 the onset of widespread deoxygenation in the oceans, changes the Tl elemental and isotopic budget
726 are the first systems to be perturbed (20). To assess the global dynamics of oceanic oxygenation
727 during the Early Jurassic, this study utilizes a novel isotopic system that is not fractionated by
728 biological processes in the open ocean (23). Thallium has two naturally occurring isotopes: ²⁰³Tl
729 and ²⁰⁵Tl. The thallium isotopic composition of a sample is compared to the NIST SRM 997 Tl
730 standard and reported such that:

$$731 \quad \epsilon^{205}\text{Tl} = 10,000 \times \left(\frac{{}^{205}\text{Tl}/{}^{203}\text{Tl}_{\text{sample}} - {}^{205}\text{Tl}/{}^{203}\text{Tl}_{\text{SRM 997}}}{({}^{205}\text{Tl}/{}^{203}\text{Tl}_{\text{SRM 997}})} \right) \quad \text{Eq. 3}$$

732 To track manganese oxide burial during the Early Jurassic, chemical analysis (21, 22) was
733 utilized to isolate thallium in a state-of-the-art clean laboratory at the National High Magnetic
734 Field Laboratory at Florida State University. For this procedure, approximately 0.05 grams of
735 sample powder (0.1 grams of standard SCO-1) was placed into a trace metal clean teflon savillex
736 beaker with 3mL of 2M HNO₃ was added and placed on a hot plate for approximately 12 hours at
737 130° C. These samples were then centrifuged, and the supernatant was collected and placed in a
738 new, clean savillex beaker, and dried. Care was taken to not collect siliciclastic materials, and to
739 ensure limited siliciclastic Tl contamination HF was avoided. Several high-purity acid treatments
740 (aqua regia, 50% conc. HCl or HNO₃ + H₂O₂) were added to each beaker to fully oxidize any
741 organic matter present. These solutions were placed on hot plates at 120-130° C for several days
742 if necessary. To completely oxidize samples for column chemistry, 1 M HCl and ~100 μL
743 brominated H₂O were added to each beaker the previous night. All acids and reagents were trace
744 metal grade to ensure low blank levels.

745 For column chemistry, we followed the method of refs. 23-25 (described below), but this
746 dataset only used one micro-column procedure, which was shown to work well for high Tl and
747 low Pb samples (22). For Pb removal, AG1X8 200-400 mesh resin was added to each column.
748 This was followed by the addition of solutions 0.1 ml and 1.5 ml of each HCl-SO₂, 0.1M HCl, and
749 0.1 M HCl with 1% Br₂-H₂O. Samples were loaded into the columns, followed by the addition of
750 0.1 ml and 1.5 ml solutions of 0.5 M HNO₃ – 3% Br₂-H₂O, 2.0 M HNO₃ – 3% Br₂-H₂O, and 0.1
751 M HCl – 1% Br₂-H₂O. Thallium was then collected using 0.1 ml and 1.5 ml of 0.1 M HCl-SO₂
752 solution. Importantly, H₂SO₄ was evaporated at high temperature, and each sample was dissolved
753 in a 0.1 M HNO₃ + 0.1% H₂SO₄ solution. A 10-μL aliquot of this solution was analyzed with an
754 Agilent 7500cs ICP-MS to measure Pb and Tl abundances. Using these concentration data, sample
755 concentrations were matched to within 25% of standard and spiked with an abundance of NIST
756 SRM 997 Pb standard. Thallium isotope measurements were performed on a Thermo Neptune
757 MC-ICP-MS at FSU. Approximately 90% of the samples were analyzed at least twice (some
758 samples were not replicated due to sample limitation). The average 2σ standard deviation for all
759 replicated samples is ± 0.25 epsilon units or better. The long-term average ε²⁰⁵Tl value for the
760 SCo-1 standard is -3.0 ± 0.3 and all of our SCo-1 values were within this range. Samples that had
761 reproducibility under 0.3 were displayed with an uncertainty of 0.3 (long-term reproducibility of
762 SCo-1 standard), and samples that had reproducibility above 0.3 are displayed with that specific
763 uncertainty.

764 **Supplementary Text**

765 Revised placement of Pliensbachian-Toarcian boundary at East Tributary section

766 The original placement of the Pliensbachian-Toarcian boundary at East Tributary was
767 placed at ~10.15 m based on the first appearance of the Toarcian ammonites *Cleviceras exaratum*
768 and *Hildaites cf. murleyi* (1). However, the boundary could feasibly occur between ~8.5 m and
769 10.15 m, as this interval also includes ammonites that are known to span the Pliensbachian-
770 Toarcian boundary in western North America (i.e., *Tiltoniceras cf. antiquum* and
771 *Protogrammoceras paltum* (27, 28). Regardless of boundary placement our interpretations remain
772 consistent in that water column deoxygenation predated the large negative CIE of the T-OAE,
773 rather occurring at the Pliensbachian-Toarcian boundary over a time-frame that is coeval with
774 phase 3 of the multi-phased Pliensbachian-Toarcian mass extinction (29) and supported by
775 osmium isotope geochemical records (2, 30) and the absolute ages of the Pliensbachian-Toarcian
776 boundary (2, 31, 32). Therefore, deoxygenation would still be considered as a major driver for the

777 main phase of this mass extinction event.

778

779 Positive carbon isotope excursion during the early Toarcian (pre-T-OAE CIE)

780 In Fig. 1 of the main text, the long-term, globally observed positive carbon isotope
781 excursion during the early Toarcian is noted. This phenomenon is observed in inorganic and
782 organic matter of marine and terrestrial carbon in several locations from Europe, Africa, and North
783 America (1, 33-39) (Fig. S3). The new thallium isotope dataset from western Canada suggest that
784 increased anoxia and burial of organic carbon were the mechanisms behind the long-term positive
785 CIE beginning in the basal Toarcian.

786

787 Ammonite zones of new oceanic deoxygenation records

788 New Tl data from two geographically far removed anoxic basins suggest that the expansion
789 of early Toarcian anoxic bottom began at the base of the correlative Tenuicostatum (northwest
790 Europe and South America), Polymorphum (Mediterranean), Antiquum (High-Arctic), and
791 Kanense (western North America) zones, and continued into the middle Toarcian at a correlative
792 level with the Bifrons Zone of northwest Europe (see ref. 29).

793

794 Dotternhausen Quarry Tl isotopes

795 In Fig. 2 of the main text, several Tl isotope data points below the T-OAE CIE were
796 displayed as light gray. These samples came from carbonate marls with extremely low TOC
797 contents (0.34 – 0.78%) (4). Therefore, we compared only the two Tl isotope data points from the
798 organic-rich black shales (pre-T-OAE) with the organic-rich black shales from the OAE and post-
799 OAE interval. Interpreting the Tl-isotopic composition of the low TOC marls as a proxy for relative
800 global manganese oxide burial is unexplored and could lead to erroneous conclusions as the Tl-
801 isotope proxy (and other metal isotope proxies) have not been developed or tested in such
802 depositional environments.

803

804 Yorkshire, UK Tl isotopes

805 The Tl-isotope results from our two new study sites cannot be directly compared with that
806 of Yorkshire, UK (42). This is because of the interpreted severe basinal restriction that
807 accompanied the T-OAE interval in the Cleveland Basin (43). The basinal restriction associated
808 with this interval is demonstrated to have overprinted rhenium, osmium, and molybdenum
809 systems, which has resulted in isotope stratigraphies that were not indicative of the global record
810 (2, 4, 30, 43). Furthermore, the larger variations in the Tl-isotopes at Yorkshire (42) compared to
811 western North America and Germany (this study) suggest the record is related to regional or local
812 Mn-oxide burial events not well connected with the open ocean.

813

814

815

816

817

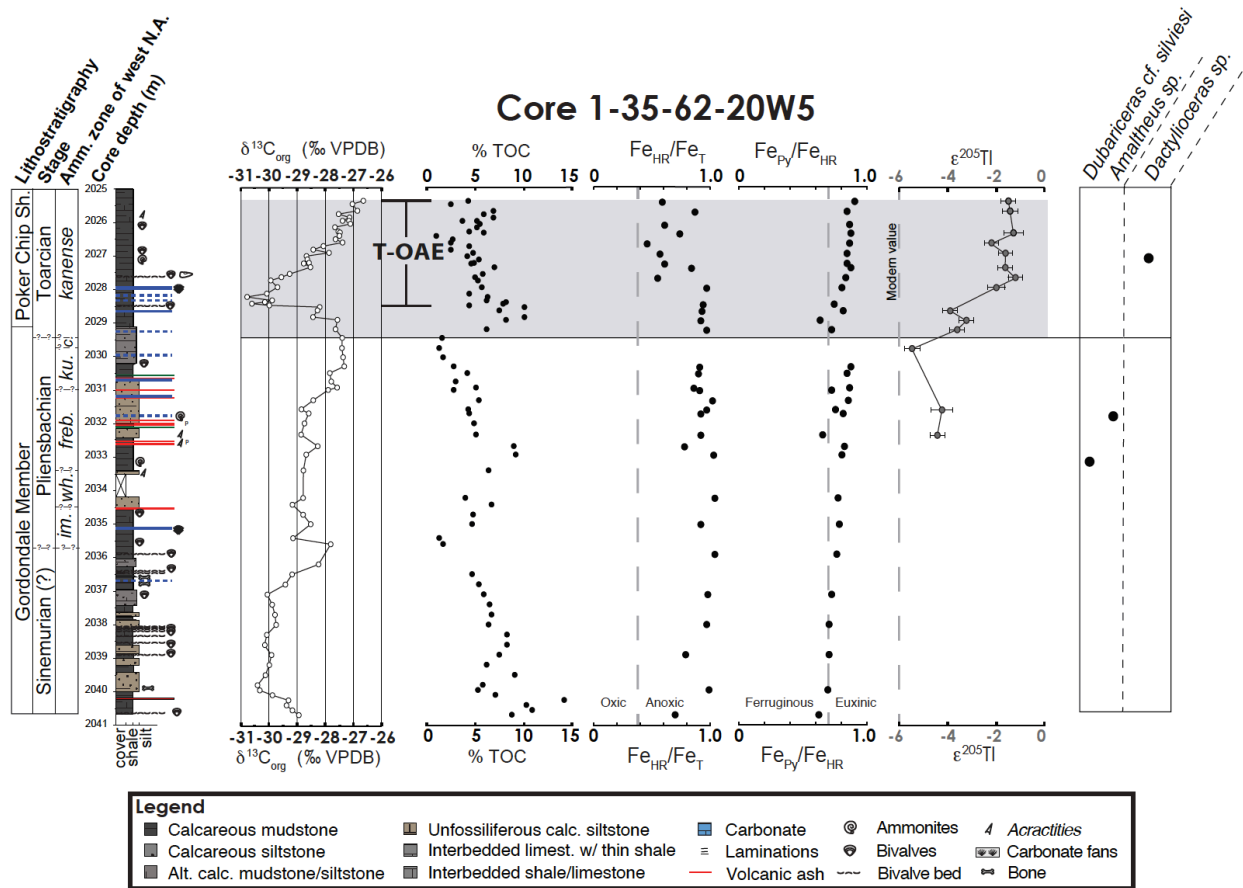
818

819

820

821

822



823

824 **Fig. S1.**

825 **Litho- and Chemo-stratigraphies of the Lower Jurassic Fernie Formation from drill core 1-**
 826 **35-62-20W5, Alberta, Canada.** $\delta^{13}C_{org}$ = organic carbon isotopic compositions. Fe_{HR}/Fe_T =
 827 amount of highly reactive iron relative to total iron, and Fe_{Py}/Fe_{HR} = amount of pyrite iron relative
 828 to highly reactive iron (see SI Materials and Methods for discussion of this local redox proxy).
 829 $\epsilon^{205}Tl_{SW}$ = thallium isotopic composition of seawater during deposition. Lithostratigraphic
 830 members of the Fernie Formation, Stages of the Jurassic, and ammonite zonation for both
 831 northwestern Europe and western North American shown to the left of the stratigraphic column.
 832 Gray bar represents approximate expansion of deoxygenated bottom waters near the Pl-To
 833 boundary.

834

835

836

837

838

839

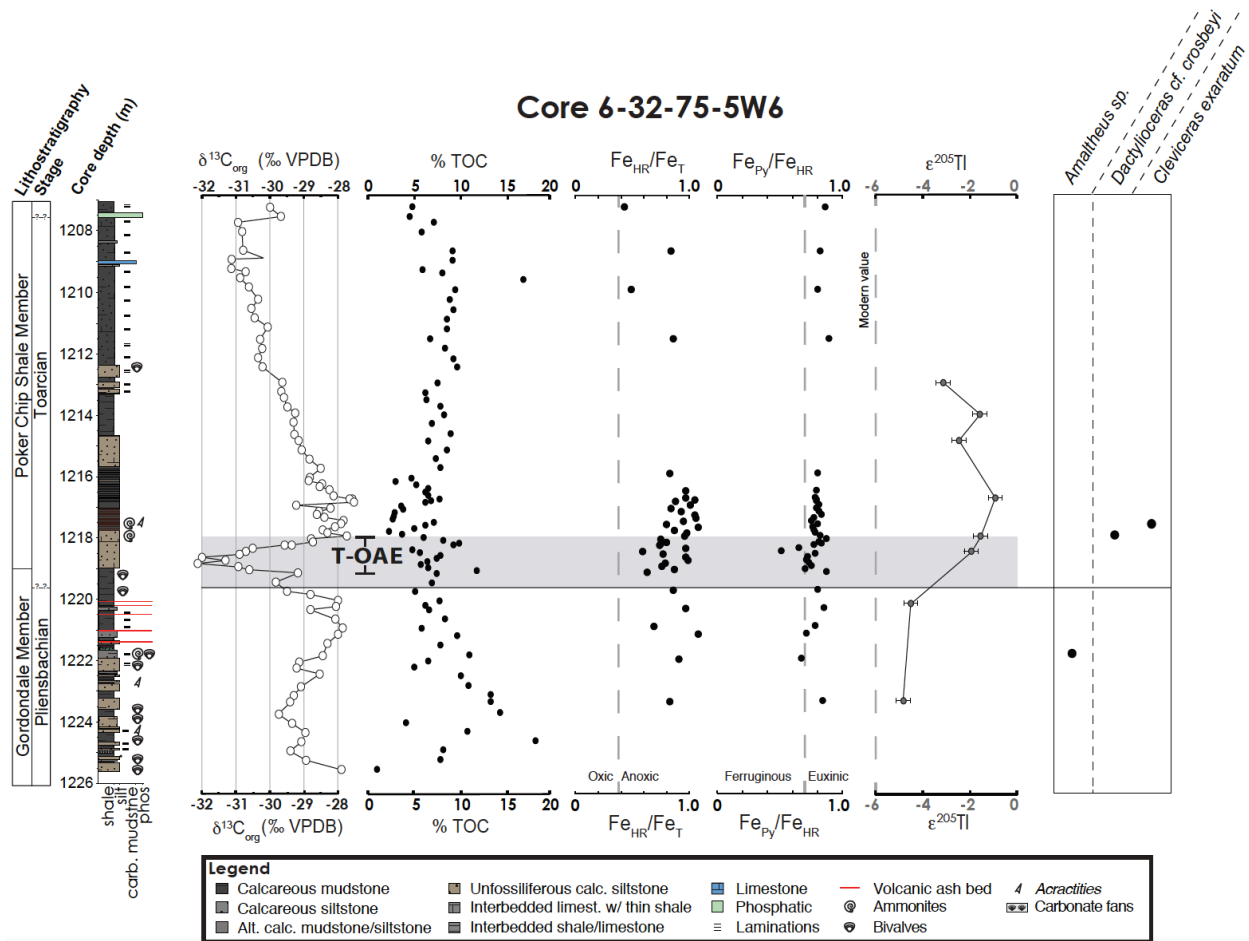
840

841

842

843

844



845

846 **Fig. S2.**

847 **Litho- and Chemo-stratigraphies of the Lower Jurassic Fernie Formation from drill core 6-**
 848 **32-78-5W6, Alberta, Canada.** $\delta^{13}C_{org}$ = organic carbon isotopic compositions. Fe_{HR}/Fe_T =
 849 amount of highly reactive iron relative to total iron, and Fe_{Py}/Fe_{HR} = amount of pyrite iron relative
 850 to highly reactive iron. $\epsilon^{205}Tl_{sw}$ = thallium isotopic composition of seawater during deposition.
 851 Lithostratigraphic members of the Fernie Formation, Stages of the Jurassic, and ammonite
 852 zonations for both northwestern Europe and western North American shown to the left of the
 853 stratigraphic column.

854

855

856

857

858

859

860

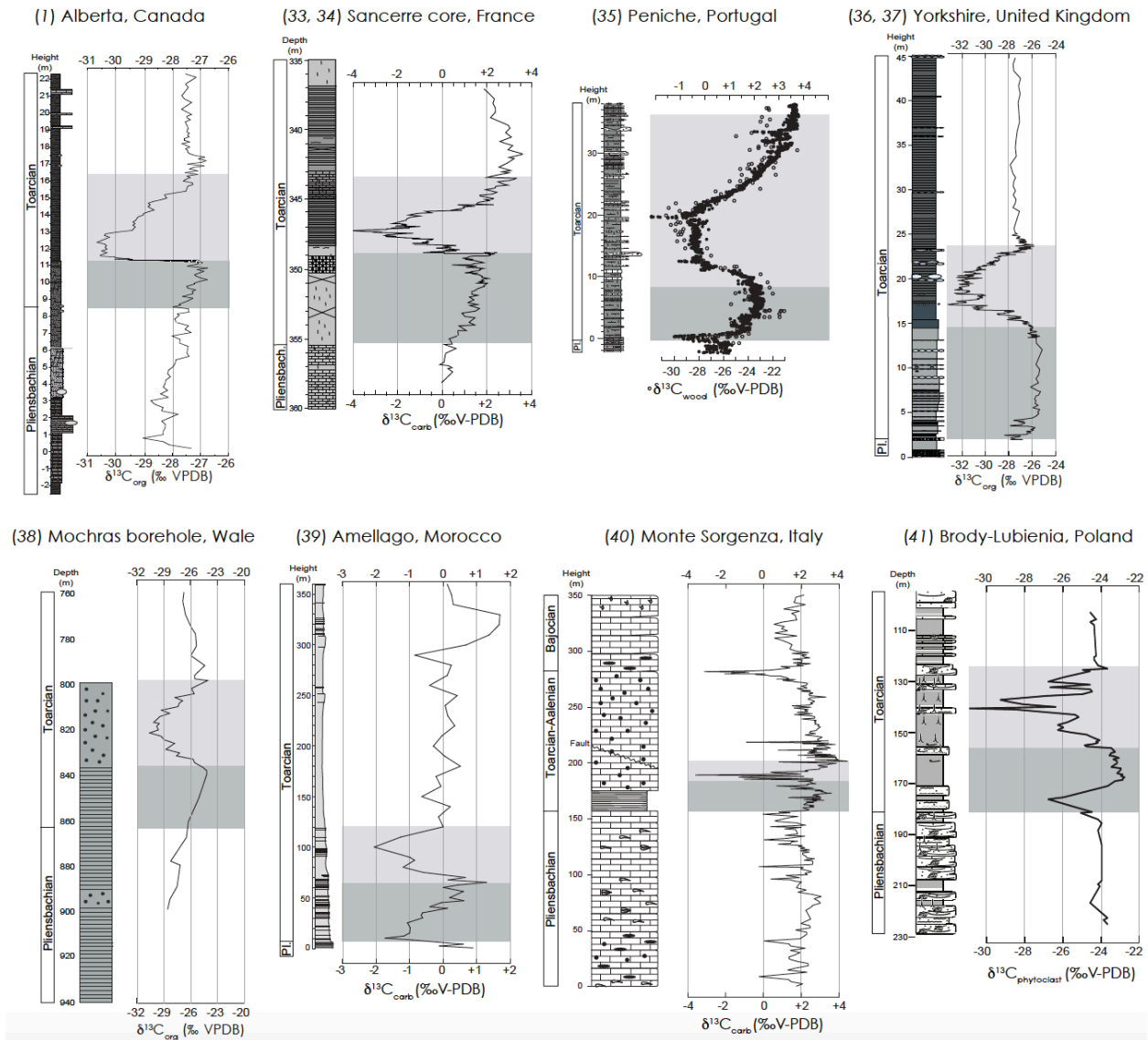
861

862

863

864

865



866

867

Fig. S3.

868

Carbon-isotope chemostratigraphies of the Pliensbachian and Toarcian stages from multiple

869

locations. $\delta^{13}\text{C}_{\text{org}}$ = organic carbon isotopic compositions; $\delta^{13}\text{C}_{\text{carb}}$ = inorganic carbon isotopic

870

compositions; $\delta^{13}\text{C}_{\text{wood}}$ and $\delta^{13}\text{C}_{\text{phytoclast}}$ = organic carbon isotopic compositions of terrestrial plant

871

wood. These carbon-isotope records all display and long-term positive $\delta^{13}\text{C}$ trend in the early

872

Toarcian until the pronounced negative CIE associated with the T-OAE (1, 33-39). Dark gray box

873

represents this long-term positive CIE. Light gray box represents the T-OAE CIE. The TI isotope

874

record suggests that the increased geographical extent of anoxia increased and resulted in the burial

875

of organic carbon (^{13}C -depleted) and ultimately the globally observed trend in higher $\delta^{13}\text{C}$ values

876

leading up to the T-OAE.

877

878

879

880

881 **Additional Data table S1 (separate file)**

882 Iron speciation and thallium isotope data from the East Tributary section.

883

884 **Additional Data table S2 (separate file)**

885 Carbon isotope, total organic carbon (TOC), iron speciation, and thallium isotope data from drill
886 core 1-35-62-20W5.

887

888 **Additional Data table S3 (separate file)**

889 Carbon isotope, total organic carbon (TOC), iron speciation, and thallium isotope data from drill
890 core 6-32-75-5W6.

891

892 **Additional Data table S4 (separate file)**

893 Iron speciation and thallium isotope data from the Dotternhausen section.

894

895

896

897

898

899

900

901

902

903

904

905

906

907

908

909

910

911

912

913

914

915

916

917

918

919

920

921

922

923

924 References

- 925 1. Them TR II, et al. (2017) High-resolution carbon isotope records of the Toarcian Oceanic
926 Anoxic Event (Early Jurassic) from North America and implications for the global drivers of
927 the Toarcian carbon cycle. *Earth Plan Sci Lett* 459:118–126.
- 928 2. Them TR, et al. (2017) Evidence for rapid weathering response to climatic warming during the
929 Toarcian Oceanic Anoxic Event. *Sci Rep* 7:5003.
- 930 3. Röhl H-J, Schmid-Röhl A, Oschmann W, Frimmel A, Schwark L (2001) The Posidonia Shale
931 (Lower Toarcian) of SW-Germany: an oxygen-depleted ecosystem controlled by sea level
932 and palaeoclimate. *Palaeogeog Palaeoclim Palaeoecol* 169:273–299.
- 933 4. Dickson AJ, et al. (2017) Molybdenum isotope chemostratigraphy and paleoceanography of the
934 Toarcian Oceanic Anoxic Event (Early Jurassic). *Paleocean* 32:813–829.
- 935 5. Asgar-Deen M, Hall R, Craig RJ, Riediger C (2003) New biostratigraphic data from the Lower
936 Jurassic Fernie Formation in the subsurface of west-central Alberta and their stratigraphic
937 implications. *Can J Earth Sci* 40:45-63.
- 938 6. Hall RL, Poulton TP, Monger JWH, Field trip A1: Calgary – Vancouver in *Field Guide for the*
939 *Fifth International Symposium on the Jurassic System, Vancouver*, Smith PL, Ed. (Jurassic
940 Sumcomission of the Stratigraphic Commission on the International Union of Geological
941 Sciences, Vancouver, 1998), chap. 2, pp. 29–61.
- 942 7. Poulton SW, Raiswell R (2002) The low-temperature geochemical cycle of iron: From
943 continental fluxes to marine sediment deposition. *Amer J Sci* 302:774–805.
- 944 8. Lyons TW, Severmann S (2006) A critical look at iron paleoredox proxies: New insights from
945 modern euxinic marine basins. *Geochim Cosmochim Acta* 70:5698–5722.
- 946 9. Canfield DE, Poulton SW, Narbonne GM (2007) Late-Neoproterozoic Deep-Ocean
947 Oxygenation and the Rise of Animal Life. *Sci* 315:92–95.
- 948 10. Poulton SW, Canfield DE (2005) Development of a sequential extraction procedure for iron:
949 implications for iron partitioning in continentally derived particulates. *Chem Geol* 214:209–
950 221.
- 951 11. Poulton SW, Canfield DE (2011) Ferruginous conditions: A dominant feature of the ocean
952 through Earth’s history. *Elem* 7:107–112.
- 953 12. Berner RA (1984) Sedimentary pyrite formation: An update. *Geochim Cosmochim Acta*
954 48:605–615.
- 955 13. Raiswell R, Newton R, Wignall PB (2001) An Indicator of Water-Column Anoxia: Resolution
956 of Biofacies Variations in the Kimmeridge Clay (Upper Jurassic, U.K.). *J Sed Res* 71:286–
957 294.
- 958 14. März C, Poulton SW, Beckmann B, Küster K, Wagner T, Kasten S (2008) Redox sensitivity
959 of P cycling during marine black shale formation: Dynamics of sulfidic and anoxic, non-
960 sulfidic bottom waters. *Geochim Cosmochim Acta* 72:3703–3717.
- 961 15. Poulton SW, et al. (2015) A continental-weathering control on orbitally driven redox-nutrient
962 cycling during Cretaceous Oceanic Anoxic Event 2. *Geol* 43:963–966.
- 963 16. Stookey LL (1970) Ferrozine – A New Spectrophotometric Reagent for Iron. *Analy. Chem.*
964 42:779–781.
- 965 17. Sperling EP, Halverson GP, Knoll AH, Macdonald FA, Johnston DT (2013) A basin redox
966 transect at the dawn of animal life. *Earth Plan Sci Lett* 371-372:143–155.
- 967 18. Canfield DE, Raiswell R, Westrich JT, Reaves CM, Berner RA (1986) The use of chromium
968 reduction in the analysis of reduced inorganic sulfur in sediments and shales. *Chem Geol*
969 54:149–155.

- 970 19. Aller RC, Mackin JE, Cox RT, Jr (1986) Diagenesis of Fe and S in Amazon inner shelf muds:
971 apparent dominance of Fe reduction and implications for the genesis of ironstones. *Cont Shelf*
972 *Res* 6:263–289.
- 973 20. Rue EL, Smith GJ, Cutter GA, Bruland KW (1997) The response of trace element redox
974 couples to suboxic conditions in the water column. *Deep Sea Res Part I: Ocean Res Pap*
975 44:113–134.
- 976 21. Owens JD, Nielsen SG, Horner TJ, Ostrander CM, Peterson LC (2017) Thallium-isotopic
977 compositions of euxinic sediments as a proxy for global manganese-oxide burial. *Geochim*
978 *Cosmochim Acta* 213:291–307.
- 979 22. Ostrander CM, Owens JD, Nielsen SG (2017) Constraining the rate of oceanic deoxygenation
980 leading up to a Cretaceous Oceanic Anoxic Event (OAE-2: ~94 Ma). *Sci Adv* 3:e1701020.
- 981 23. Rehkämper M, Halliday AN (1999) The precise measurement of Tl isotopic compositions by
982 MC-ICPMS: Application to the analysis of geological materials and meteorites. *Geochim*
983 *Cosmochim Acta* 63:935–944.
- 984 24. Nielsen SG, Rehkämper M, Baker J, Halliday AN (2004) The precise and accurate
985 determination of thallium isotope compositions and concentrations for water samples by MC-
986 ICPMS. *Chem Geol* 204:109–124.
- 987 25. Baker RGA, Rehkämper M, Hinkley TM, Nielsen SG, Toutain JP (2009) Investigation of
988 thallium fluxes from subaerial volcanism – Implications for the present and past mass balance
989 of thallium in the oceans. *Chem Geol* 73:6340–6359.
- 990 27. Caruthers AH, Smith PL (2012) Pliensbachian ammonoids from the Talkeetna Mountains
991 (Peninsular Terrane) of Southern Alaska. *Rev de Paléo Gen* 11:365–378.
- 992 28. Caruthers AH, Gröcke DR, Smith PL (2011) The significance of an Early Jurassic (Toarcian)
993 carbon-isotope excursion in Haida Gwaii (Queen Charlotte Islands), British Columbia,
994 Canada. *Earth Plan Sci Lett* 307:19–26.
- 995 29. Caruthers AH, Smith PL, Gröcke DR (2013) The Pliensbachian-Toarcian (Early Jurassic)
996 extinction, a global multi-phased event. *Palaeogeog Palaeoclim Palaeoecol* 386:104–118.
- 997 30. Percival LME, et al. (2016) Osmium isotope evidence for two pulses of increased continental
998 weathering linked to Early Jurassic volcanism and climate change. *Geol* 44:759–762.
- 999 31. Sell B, et al. (2014) Evaluating the temporal link between the Karoo LIP and climatic—
1000 biologic events of the Toarcian Stage with high-precision U-Pb geochronology. *Earth Plan*
1001 *Sci Lett* 408:48–56.
- 1002 32. Ruhl M, et al. (2016) Astronomical constraints on the duration of the Early Jurassic
1003 Pliensbachian Stage and global climate fluctuations. *Earth Plan Sci Lett* 455:149–165.
- 1004 33. Hermoso M, Le Callonnec L, Minoletti F, Renard M, Hesselbo SP (2009) Expression of the
1005 Early Toarcian negative carbon-isotope excursion in separated carbonate microfractions
1006 (Jurassic, Paris Basin). *Earth Plan Sci Lett* 277:194–203.
- 1007 34. Hermoso M, et al. (2012) Dynamics of a stepped carbon-isotope excursion: Ultra high-
1008 resolution study of Early Toarcian environmental change. *Earth Plan Sci Lett* 319-320:45–
1009 54.
- 1010 35. Hesselbo SP, Jenkyns HC, Duarte LV, Oliveira LCV (2007) Carbon-isotope record of the Early
1011 Jurassic (Toarcian) Oceanic Anoxic Event from fossil wood and marine carbonate (Lusitanian
1012 Basin, Portugal). *Earth Plan Sci Lett* 253:455–470.
- 1013 36. Kemp DB, Coe AL, Cohen AS, Schwark L (2005) Astronomical pacing of methane release in
1014 the Early Jurassic period. *Nature* 437:396–399.
- 1015 37. Littler K, Hesselbo SP, Jenkyns HC (2011) A carbon-isotope perturbation at the

- 1016 Pliensbachian-Toarcian boundary: evidence from the Lias Group, NE England. *Geol Mag*
1017 147:181–192.
- 1018 38. Jenkyns HC, Gröcke DR, Hesselbo SP (2001) Nitrogen isotope evidence for water mass
1019 denitrification during the early Toarcian (Jurassic) oceanic anoxic event. *Paleocean* 16:593–
1020 603.
- 1021 39. Bodin S, et al. (2010) Toarcian carbon isotope shifts and nutrient changes from the Northern
1022 margin of Gondwana (High Atlas, Morocco, Jurassic): Palaeoenvironmental implications,
1023 *Palaeogeog Palaeoclim Palaeoecol* 297:377–390.
- 1024 40. Woodfine RG, Jenkyns HC, Sarti M, Baroncini F, Violante C (2008) The response of two
1025 Tethyan carbonate platforms to the early Toarcian (Jurassic) oceanic anoxic event:
1026 environmental change and differential subsidence. *Sediment* 55:1011–1028.
- 1027 41. Hesselbo SP, Pieńkowski G (2011) Stepwise atmospheric carbon-isotope excursion during
1028 the Toarcian Oceanic Anoxic Event (Early Jurassic, Polish Basin). *Earth Plan Sci Lett*
1029 301:365–372.
- 1030 42. Nielsen SG, et al. (2011) Thallium isotopes in early diagenetic pyrite – A paleoredox proxy?
1031 *Geochim Cosmochim Acta* 75:6690–6704.
- 1032 43. McArthur JM, Algeo TJ, vd Schootbrugge B, Li Q, Howarth RJ (2008) Basinal restriction,
1033 black shales, Re-Os dating, and the Early Toarcian (Jurassic) oceanic anoxic event.
1034 *Paleocean* 23:PA4217.